Materials Today Bio 29 (2024) 101330

Contents lists available at ScienceDirect

Materials Today Bio

journal homepage: www.journals.elsevier.com/materials-today-bio

Engineered biomimetic nanovesicles-laden multifunctional hydrogel enhances targeted therapy of diabetic wound

Shuoyuan Liu [a,1], Gui Wan [a,1], Tao Jiang [a], Chengqi Yan [a], Guoyong Jiang [a], Maojie Zhang [b], Kaituo Xiang [c], Chi Zhang [a], Xuejiao Xiang [d], Huayuan Zhao [e], Chengcheng Li [a], Zhichao Ruan [a], Yangyang Chen [f], Yanhua Chen [a,***], Xiaofan Yang [a,**], Zhenbing Chen [a,*]

[a] Department of Hand Surgery, Union Hospital, Tongji Medical College, Huazhong, University of Science and Technology, Wuhan, 430022, China
[b] Department of Thyroid and Breast Surgery, The Central Hospital of Wuhan, Tongji Medical College, Huazhong University of Science and Technology, Wuhan, Hubei, China
[c] Department of Orthopaedics, The Second Affiliated Hospital and Yuying Children's Hospital of Wenzhou Medical University, Wenzhou, 325027, China
[d] Department of Disease Control and Prevention, Shanghai Changzheng Hospital, 200003, Shanghai, China
[e] Department of Urology, Union Hospital, Tongji Medical College, Huazhong, University of Science and Technology, Wuhan, 430022, China
[f] Department of Obstetrics and Gynecology, Union Hospital, Tongji Medical College, Huazhong University of Science and Technology, Wuhan, 430022, China

ARTICLE INFO

Keywords:
Biomedical engineering
Stem cell
Nanovesicles
Targeted delivery
Hydrogel
Synergistic therapeutics
Diabetic wound healing

ABSTRACT

Angiogenesis is essential for diabetic wound healing. Endothelial progenitor cell-derived extracellular vesicles (EPC-EVs) are known to promote wound healing by enhancing angiogenesis, while the low yield and lack of effective targeting strategies limit their therapeutic efficacy. Here, the biomimetic nanovesicles (NVs) prepared from EPC (EPC-NV) through an extrusion approach were reported, which functioned as EV mimetics to deliver contents from EPC to the wound. Besides, the cRGD peptide was coupled to the surface of EPC-NV (mEPC-NV) to achieve active endothelial cells (ECs)-targeting. Furthermore, we developed a dual hydrogel network by combining Fe^{3+}@ Protocatechualdehyde (PA) complex-modified Acellular Dermal Matrix (ADM) with light-cured gelatin (GelMA), to enrich and sustainably release mEPC-NV. The hydrogel system with antioxidant and antibacterial properties also made up for the deficiency of mEPC-NV, reducing reactive oxygen species (ROS) and inhibiting infection in diabetic wound. Taken together, this study established a novel bioactive delivery system with angiogenesis, antioxidant and antibacterial activities, which might be a promising strategy for the treatment of diabetic wound.

1. Introduction

Diabetes represents a globally prevalent and severe chronic metabolic disorder [1]. Chronic non-healing diabetic wounds, especially diabetic foot ulcers, are prevalent complications of diabetes, imposing substantial health and financial burdens on millions globally [2–4]. Although various treatment methods, including biomaterials, drugs, and stem cells, have been developed to aid diabetic wound healing, approximately 25 % of diabetic patients still undergo limb amputation due to prolonged wound healing, and the 5-year mortality rate following amputation exceeds 70 % [5]. Therefore, the identification of effective treatments for diabetic wound healing represents an urgent unmet need [6–8].

Adequate vascularization plays a crucial role in wound healing by facilitating the delivery of essential nutrients and oxygen to the injured tissue, thereby creating a conducive microenvironment for the repair process [9–11]. In diabetic wounds, hyperglycemia-induced endothelial dysfunction impairs angiogenesis, which is an important cause of delayed wound healing. Many studies have showed that impaired angiogenesis in diabetic wounds can lead to hypoxia, nutrient

* Corresponding author.
** Corresponding author.
*** Corresponding author. Department of Hand Surgery, Union Hospital, Tongji Medical College, Huazhong University of Science and Technology, 1277 Jiefang Ave, Wuhan, 430022, China.
E-mail addresses: chenyanhua1977@163.com (Y. Chen), 2017xh0119@hust.edu.cn (X. Yang), 1993xh0571@hust.edu.cn (Z. Chen).
[1] Contributed equally.

https://doi.org/10.1016/j.mtbio.2024.101330
Received 7 July 2024; Received in revised form 16 October 2024; Accepted 6 November 2024
Available online 7 November 2024

deprivation, impaired immune cell recruitment, disrupted stem cell homing, reduced growth factor delivery, and chronic inflammation [12–15]. Therefore, there is an urgent need for more effective strategies to promote angiogenesis in the treatment of diabetic wounds [16,17]. Evidences indicate that endothelial progenitor cell (EPC)-derived extracellular vesicles (EVs) can enhance angiogenesis and facilitate wound healing in hypoxic environments [18–22]. However, low yield and high cost are key barriers to the application of this approach in practice [23–25]. Recently, studies have been conducted on an extrusion approach to the preparation of nanovesicles (NVs) as mimetics for EVs [26–28]. NVs prepared by the serial extrusion of cells have comparable cell membranes and are similar in size to EVs, and are more enriched in proteins and RNAs than EVs, resulting in a higher yield [29]. Accordingly, compared to EVs, NVs may exhibit superior efficacy in facilitating biomolecule delivery and eliciting therapeutic responses within recipient cells.

In this study, EPC-NVs were not only taken up by trabecular human umbilical vein endothelial cells (HUVECs) but also fibroblasts (HDF) and keratinocytes (HaCaT). Importantly, EPC-NVs are internalized by HDF and HaCaT cells without significantly influencing their proliferation or migration, whereas they notably promote angiogenesis in endothelial cells (ECs). Therefore, an engineering strategy is necessary to improve the targeting ability of EPC-NVs. Previous studies suggested that the small molecule peptide arginine-glycine-aspartate sequence (RGD peptide) can specifically bind to the endothelial integrin αvβ3 on EC membranes [30]. Moreover, cyclic RGD peptide (cRGD) has stronger specificity and affinity for integrin αvβ3 than linear RGD peptide, and is more stable *in vivo* [31–33]. This method has been widely used in research for the treatment of cancer [34–39]. Hence, we coupled cRGD to the surface of EPC-NVs (mEPC-NV) to achieve active targeting of ECs by EPC-NV.

Although the therapeutic effect of biomimetic NVs in diabetic trauma has been demonstrated, there remain issues with their application in practice. Traditionally, EV-related treatments are administered via injection, either a single injection for large-dose or multiple injections for low dose [40]. However, using these methods, EVs may be phagocytosed by macrophages due to excessive EV concentrations in patients receiving large doses, and complications may occur in patients receiving multiple low-dose injections [41]. Furthermore, elevated levels of oxidative stress and susceptibility to bacterial infections are also present in diabetic wounds [42–44]. As such, single mEPC- NV therapy may be associated with suboptimal therapeutic outcomes. To address these issues, we propose a dual hydrogel namely ADM-Fe^{3+}@PA/GelMA (AFG) that allows loading of mEPC-NVs in large quantities, which reduces reactive oxygen species (ROS) levels and inhibits bacterial infection.

Multiple factors affect the healing of diabetic wounds, and an effective therapeutic approach should address as many of these as possible. This study aims to tackle three crucial factors contributing to suboptimal diabetic wound healing; 1) impaired EC function, 2) increased oxidative stress, 3) vulnerability to bacterial infection. To do this, we developed a multifunctional hydrogel named AFG-mNV (ADM-Fe^{3+}@PA-mNV/GelMA), demonstrating excellent biocompatibility and sustained release of mEPC-NVs (mNV) with EC-targeting ability. This system promotes diabetic wound healing by enhancing angiogenesis, scavenging reactive oxygen species (ROS), and inhibiting bacterial infection.

2. Methods

2.1. Manufacture and isolation of nanovesicles

The EPC-NVs (NVs) were prepared and purified using a well-established extrusion method [45]. Briefly, EPCs cultured *in vitro* were dissociated utilizing TrypLE™ Express Enzyme (Gibco, USA), and subsequently, diluted to a concentration of 5×10^6 cells mL^{-1} using PBS (Gibco, USA). The cell suspension was then passed through a mini-extruder (Avanti Polar Lipids, USA) across a sequence of Nuclepore™ track-etched polycarbonate membranes (Whatman, USA) with pore sizes of 10 μm, 5 μm, 1 μm, and 0.4 μm, each iteration being repeated five times (Fig. 1A).

Following extrusion, the samples were subjected to centrifugation at 3000×*g* for 20 min and 9000×*g* for 30 min at 4 °C to remove cells, debris, and microvesicles. Next, the supernatant was centrifuged at 140000×*g* for 90 min at 4 °C to isolate nanoscale vesicles. The vesicle pellets underwent two washes, were resuspended in cold sterile PBS, and stored at −80 °C for future use within one month.

2.2. Engineering and characterization of cRGD-NV

The phospholipid (DSPE)-PEG2K-cRGDyK powder (0.5 mg, Xi'an Ruixibio Ltd, China) was dissolved in 0.5 mL sterile ultrapure water and co-incubated at 60 °C for 30 min to form micelles. Subsequently, 1 mL of NV suspension was incubated with 0.5 mL of cRGD micelle solution at 40 °C for 2 h, the cRGD-modified NVs were then purified by size exclusion chromatography.

To detect the positive connectivity rate between cRGD peptides and NVs, FAM (Green Fluorescent Probes, 488 nm)-cRGD@NVs were tested by Nano Flow Cytometry (NanoFCM, Fuliu Biotechnology, China).

2.3. Characterization of EPC-NV and mEPC-NV

The morphologies of EPC-NV and mEPC-NV were observed using transmission electron microscopy (TEM, Hitachi, Japan). The zeta potential was measured using nanoparticle tracking analysis (NTA, Particle Metrix, GER). The particle diameter was measured using Nano Flow Cytometry (NanoFCM, Fuliu Biotechnology, China) Western-blot was utilized to evaluate the expression of EVS markers such as CD9, CD81, TSG101.

2.4. Cellular uptake assay

Cells were seeded in 24-well culture plates (8000-10000 cells per well) and were co-incubated with 20 μg/mL DiI (Beyotime, China)-labeled NVs for 24 h. Following the incubation period, cells were rinsed 2–3 times with PBS and subsequently fixed with 4 % paraformaldehyde for 20 min. Then, cell cytoskeletons were stained with FITC (HYCEZBIO, China) phalloidin and cell nucleics were stained with DAPI (Solarbio, Beijing, China). The images of NVs internalization by cells were visualized and imaged with confocal laser scanning microscopy (CLSM, Nikon, Japan)) and quantified by ImageJ. The cellular uptake was expressed as amount of DiI-labeled NVs/total cell amount × 100 %.

2.5. Cellular proliferation, migration, tube formation assay

Cellular proliferation was evaluated using EdU staining (Beyotime, China). The Transwell migration assay was used to evaluate the migration ability of cells (24-well Transwell Chamber, Corning, USA). Briefly, serum-starved cells (20,000 cells/well) were seeded into the upper compartment of transwells and incubated for 24 h with a complete medium containing 10 % FBS in the lower chamber. Migrated cells on the bottom surface were stained with crystal violet (Solarbio, Beijing, China) and counted microscopically. For tube formation, HUVECs (30,000 cells/well) were seeded on coated with 65 μL Matrigel Basement Membrane Matrix (BD Biosciences, CA, USA)-coated 96-well plates. After 6 h incubation, tube formation was imaged, and junction points were quantified using the ImageJ angiogenesis plugin.

2.6. EC-targeting ability in vitro

GFP-labeled HUVECs were co-cultured with HaCaT or HDF cells in 24-well culture plates to establish an *in vitro* cutaneous cell model. DiI-

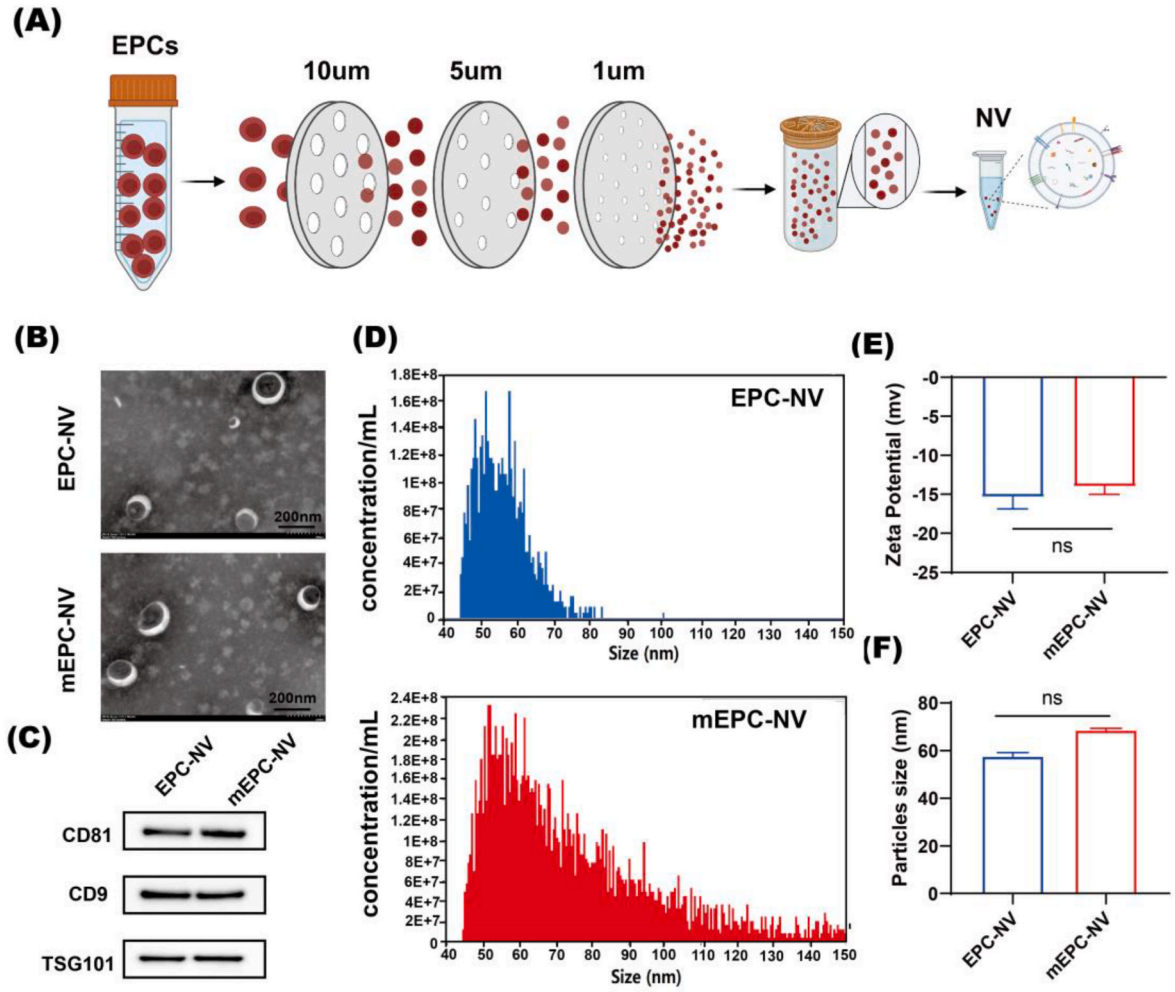

Fig. 1. Manufacture and characterization of EPC-NV and mEPC-NV.
(A) Schematic diagram of NVs manufacture. **(B)** TEM image of EPC-NV and mEPC-NV. Scale bar: 200 nm. **(C)** Western blotting analysis of EVs specific markers including CD9, CD81 and TSG101 of EPC-NV and mEPC-NV. **(D)** and **(F)** Show the results of size distribution of EPC-NV and mEPC-NV. **(E)** Show the zeta potential of EPC-NV and mEPC-NV. (ns indicates no significant).

labeled NVs were internalized as described earlier. The targeting efficiency of NVs was evaluated based on the distribution relationship between DiI and GFP, calculated using the following equation:

$$\text{Target efficiency}\ (\%) = \frac{\frac{1}{m}\sum_{i=m} F_i}{\frac{1}{n}\sum_{j=n} F_j} \times 100\%$$

The red fluorescence signal in GFP-labeled HUVEC and other cells (HaCaT or HDF) was represented as Fi and Fj, respectively. Targeting efficiency was assessed using ImageJ software.

For flow cytometry (FCM), HUVECs were seeded in 6-well culture plates for 12 h, after treated by PBS or MGO for another 24 h, they were co-cultured with Dil-labeled NVs or Dil-labeled mNVs with the same quality for 24 h. Subsequently, the cells were rinsed twice with PBS and collected into flow tubes after digestion with trypsin. The cellular uptake of NVs was evaluated by quantifying the mean fluorescence intensity (MFI) with a Gallios Flow Cytometer (Beckman Coulter, Miami, FL, USA) following the manufacturer's protocol. FlowJo software was used for data analysis (version 10.8.1, BD biosciences).

2.7. Preparation and characterization of AFG-mNV hydrogel

The constituents, namely protocatechuic aldehyde (PA), ferric chloride hexahydrate ($FeCl_3{\cdot}6H_2O$), an acellular dermal matrix (ADM) (Youchuang, Jiangsu, China), light-curable gelatin (GelMA) (EFL, Jiangsu, China), and mEPC-NVs, were employed to fabricate hydrogels via photo-crosslinking at ambient temperature. Specifically, a Fe^{3+}@PA solution was synthesized following a prior report, blended with ADM particulates, and subsequently, redundant Fe^{3+}@PA was eliminated via centrifugation. Thereafter, a GelMA formulation incorporating 50 μg of mEPC-NVs was introduced, and gel formation was facilitated through exposure to 416 nm blue light irradiation for a duration of 10 s [46].

The hydrogel structures were characterized by scanning electron microscopy (SEM) and rheometry. Enzymatic degradation was evaluated using 2 U/mL collagenase-I, with the degradation rate determined from weight loss measurements.

$$\text{degradation rate} = \frac{(\text{Wi} - \text{Wx})}{\text{Wi}} \times 100\%$$

Here, Wi denotes the initial weight of the dry sample, and Wx signifies the weight of the dry sample degraded on day x.

The hemocompatibility of the AFG hydrogel was evaluated using a hemolysis assay. Purified red blood cells were diluted to 5 % (v/v) suspension, which was incubated with the AFG hydrogel for 4 h at 37 °C, alongside ultrapure H_2O (positive control) and PBS (negative control). After centrifugation at 2000 rpm for 10 min, the supernatant absorbance was measured at 540 nm to quantify hemolysis. The OD value of the AFG group is the actual value minus the background value.

To learn the distribution of NVs in the AFG hydrogel, the laser scanning confocal was used to observe the plan and 3D construction image of AFG-DiI-mNV.

2.8. Biocompatibility of AFG hydrogel

The biocompatibility of AFG hydrogel was assessed through CCK-8 and LIVE/DEAD assays. For the CCK-8 assay, absorbance at 450 nm was measured using a microplate reader, and cell viability was calculated as (As - Ab)/(Ac - Ab) × 100 %, where As, Ac, and Ab represent sample, control, and blank absorbance values, respectively. A leachate was prepared by soaking 0.5 g of AFG hydrogel material in 50 mL of DMEM with 10 % FBS for 24 h. Cells were exposed to the leachate for 24 h, with PBS-treated cells as controls. Subsequently, cells were stained with a Calcein-AM/PI kit (Beyotime, China) for the LIVE/DEAD assay and imaged using fluorescence microscopy.

2.9. Antibacterial ability of AFG hydrogel in vitro

The antimicrobial activity of the AFG hydrogel was assessed through colony formation assays, bacterial growth curves, and an antimicrobial ring assay. To evaluate antimicrobial activity, 100 μL of bacterial suspension at a concentration of 1×10^6 CFU/mL was spread uniformly onto an agar plate. Subsequently, sterilized paper discs (8 mm diameter) containing the hydrogel samples were placed on the inoculated plate and incubated for 24 h at 37 °C. Following incubation, the zone of inhibition surrounding the hydrogel discs was analyzed.

Bacterial suspensions of *Staphylococcus aureus (S. aureus)* and *Escherichia coli* (*E. coli)* were prepared in Luria-Bertani (LB) broth at a final concentration of approximately 1×10^6 colony-forming units per milliliter. Different treatment solutions were co-incubated with the bacterial suspension for differing durations at 37 °C. To construct the bacterial growth curve, 100 μL of the bacterial suspension was sampled at 0, 6, 12, 18, and 24 h for absorbance measurement at 600 nm. For the colony formation assay, the suspension was collected at 4 h, diluted 20-fold with PBS, and spread onto LB plates, followed by incubation at 37 °C for 24 h. Colony images were captured, and the colony count was determined using ImageJ software.

2.10. Antioxidant ability of AFG hydrogel in vitro

To detect the ROS scavenging ability of AFG hydrogel, cells (HUVEC or HDF or HaCaT) were seeded in 24-well culture plates and treated with PBS or MGO or AFG hydrogel leachate for 24 h. Then, the cells were detected by the ROS Assay kit (Beyotime, China), according to the manufacturer's instructions. Briefly, the cells were stained with DCFH-DA dye (10 μM, 500 μL/well) for 20 min, washed twice with PBS, and imaged by fluorescence microscope.

2.11. Diabetic wound model

All animal experiments received approval from the Animal Care Committee of Tongji Medical College. For a span of five consecutive days, 6-week-old male C57BL/6 mice (body weight 15–25g) received intraperitoneal injections of streptozotocin (STZ, 50 mg/kg body weight) (Biosharp, China) to induce diabetes. Two weeks later, the weights of STZ-treated mice were found lower than normal mice. The blood glucose levels of STZ-injected mice were >16.7 mM determined using a blood glucose meter, indicating the successful induction of diabetic mice models. Additional 4 weeks were needed to monitor the glucose levels before surgery. Prior to the surgical intervention, the mice were rendered unconscious through intraperitoneal administration of sodium pentobarbital anesthetic (Sigma–Aldrich) (1 %, 50 mg/kg). Under aseptic conditions, an 8-mm full-thickness wound was created in the dorsum of each mouse. Then, the diabetic mice were randomly assigned to 6 groups (n = 10/group): PBS (40 μL PBS), AFG (40 μL AFG), NV (40 μL NV, 40 μg/mL), mNV (40 μL mNV, 40 μg/mL), AFG-mNV (40 μL AFG-mNV); the Normal (40 μL PBS) group contained 10 normal mice. Another two groups were NV (40 μL DiI-labeled NV, 40 μg/mL), mNV (40 μL DiI-labeled mNV, 40 μg/mL) (n = 5/group). Each mouse was injected around the wound by multisite subcutaneous injection (four sites). In the AFG and AFG-mNV groups, the diabetic wound areas were irradiated with a blue light laser (416 nm) after adding hydrogel solution and maintained at indoor temperature for 10 s. Treatments were also performed on day 4 and day 8 post-wounding. Photographs of wound healing were captured at days 0, 4, 8, and 12, and wound areas were evaluated by ImageJ software.

2.12. Detection of wound ROS levels

In the diabetic wound model, the wound tissue samples collected on day 12 were made into frozen sections (longitudinally cut into 8 μm thick) and subjected to DHE staining. Images were taken using a fluorescence microscope and analyzed using ImageJ software.

2.13. EC-targeting ability in vivo

The DiI-labeled NV (40 μL, 40 μg/mL) and DiI-labeled mNV (40 μL, 40 μg/mL) were injected to the NV group and mNV group diabetic mice wound, respectively. The wound tissue collected on day 4 was frozen and made into longitudinal sections. Subsequently, these sections were stained with DAPI and CD31/PECAM-1 Antibody. Fluorescence microscopy images were acquired at wound center and edge (Nikon, Japan).

2.14. Histological and immunostaining analysis

The whole wound beds of mice were collected 12 days after surgery and were fixed within 4 % paraformaldehyde solution. Following dehydration using a graded ethanol series, the tissues were embedded in paraffin and subsequently sliced into longitudinal sections with a thickness of 8 μm. Hematoxylin and eosin (H&E) staining was utilized to assess the rate of re-epithelialization in the wound area, while collagen accumulation was evaluated using Masson staining.

Mature vessel formation in wound beds was determined by incubating sections overnight at 4 °C with α-SMA antibody (Abcam, USA), followed by three PBS washes and 1 h incubation with a secondary antibody (Aspen, China) at room temperature. To evaluate inflammatory responses, sections of diabetic wound samples were stained for IL-1β using immunofluorescent antibodies (Abcam, USA) overnight at 4 °C. To evaluate the neovascularization in the wound tissues, the sections were incubated with CD31 antibody (AFFinity, AUS) for immunohistochemical staining. The image was taken by a microscope and then analyzed by using ImageJ software.

2.15. Statistical analysis

All experimental data were analyzed using GraphPad Prism10 and presented as mean ± standard deviation (SD). For pairwise comparisons, an unpaired Student's t-test was employed. For comparisons involving three or more groups, one-way analysis of variance (ANOVA) with Tukey's multiple comparisons test was utilized. All *in vitro* experiments were conducted in triplicate at minimum. (ns indicates no significant, *p < 0.05, **p < 0.01, ***p < 0.001, ****p < 0.0001).

3. Results

3.1. Manufacture and characterization of EPC-NV and mEPC-NV

NVs derived from EPCs were isolated by extrusion and ultracentrifugation as described above. TEM images show that the NVs were spherical, double-membraned, and approximately 100 nm in diameter. (Fig. 1B). Nano FCM results further verified the nanoscale size of the

NVs. The diameter of EPC-NVs was approximately 54.8 ± 7.9 nm, with mEPC-NVs slightly larger at about 67.8 ± 23.8 nm (Fig. 1D and F). The zeta potential of EPC-NVs and mEPC-NVs was −15 ± 0.9 mV and −14 ± 0.6 mV, respectively (Fig. 1E). Western blotting analysis revealed high expression of EV-specific markers in both NVs including CD9, CD81, and TSG101 (Fig. 1C). Overall, our results showed that the mEPC-NVs characteristics were similar to EPC-NVs and conformed to the identification standards of EVs.

3.2. EPC-NV can promote EC function under oxidative stress

We evaluated EPC-NVs internalization by incubating 20 μg DiI-labeled EPC-NVs with HUVEC, HDF, and HaCaT, respectively. Using CLSM, we visualized red fluorescent staining in the cytoplasm of all cell types, indicating that EPC-NVs were steadily phagocytized by these cells (Fig. 2A). Previous studies have shown that EPC-NVs promote proliferation and migration, and enhance the angiogenic capacity of HUVEC under oxidative stress [47–49]. In this study, we treated HUVEC, HDF, and HaCaT cells with EPC-NVs under MGO and H_2O_2-induced oxidative stress conditions, respectively. The control group in each case was treated with PBS. Next, we assessed cell behavior through EdU assays, transwell assays, and *in vitro* tube formation assays. The results indicate that EPC-NVs partially recovered proliferation, migration, and angiogenic capacity in HUVEC cells under oxidative stress, compared with the control group (Fig. 2B–D, 2I-K, Fig. S2). We also observed that EPC-NVs failed to recover the proliferation and migration functions of HDF (Fig. 2E and F and 2L, M, Fig. S3) and HaCaT cells (Fig. 2G and H and 2N, O, Fig. S4) under oxidative stress. These results indicated that EPC-NVs can be internalized by HUVEC, HDF, and HaCaT cells, but they only promote proliferation, migration, and angiogenesis in HUVEC under oxidative stress. No significant enhancement in proliferation or migration was observed in HDF and HaCaT cells.

3.3. cRGD-modified EPC- NV achieves EC-targeting in vitro

We next considered whether modifying the cRGD targeting peptide on the surface of EPC-NVs would help to avoid wastage due to uptake by other cells and to maximize its therapeutic function. Nano FCM analysis revealed that the positive connectivity between cRGD peptides and NVs was 76.1 % (Fig. 3G), which indicates that most of the cRGD peptides were successfully attached to EPC-NVs. To assess the intracellular uptake of the mEPC-NV, DiI-labeled NVs and DiI-labeled mNVs (red) were co-incubated with HUVECs for 12 h and examined under CLSM. Some few red fluorescence was observed in HUVECs in the EPC-NV group and was notably distributed next to the nucleus (blue, DAPI-stained) in the mEPC-NV group (Fig. 3A). The cell uptake percentage in the mEPC-NV group was 82.03 %, while in the EPC-NV group was only 26.03 % (Fig. 3B). This result implied that cRGD peptides helped intensify the intracellular uptake of mEPC-NV *in vitro*, a similar outcome that was also confirmed by flow cytometry (FCM) (Fig. 3E and F). The mean fluorescence intensity (MFI) of red fluorescence in mEPC-NV group was significantly higher than that in EPC-NV group.

To further validate the targeted delivery of mEPC-NV in diabetic wounds, a cutaneous *in vitro* cell model was established. HUVECs were distinguished from HDF and HaCaT cells of fusiform or imbricate morphology by green fluorescent protein (GFP) fluorescence. Subsequently, 293T cell-derived NVs (293T-NV) were prepared as a negative control using established protocols. The 293T-NV, EPC-NV, and mEPC-NV were labeled with DiI dye. CLSM imaging was employed to evaluate the internalization of these distinct nanovesicle into GFP-labeled HUVECs ($HUVEC^{GFP}$). As shown in Fig. 3C and D, mEPC-NVs were internalized more by ECs than other typical skin cells (HDF and HaCaT), demonstrating the targeting ability of cRGD.

These data confirmed that mEPC-NV exhibited excellent EC-targeting ability which was attributed to presence of membrane cRGD peptide.

3.4. mEPC-NV restores EC function

To investigate whether mEPC-NVs could restore HUVEC proliferation, migration, and tube formation functions in diabetic wounds, we cultured HUVECs under MGO and H_2O_2-induced oxidative stress. Initially, we assessed HUVEC proliferation and noted a marked reduction in EdU-positive nuclei following PBS treatment under oxidative stress, a trend partially countered by EPC-NV. Interestingly, the number of EdU-positive nuclei significantly rose under oxidative stress following pretreatment with mEPC-NV (Fig. 4A–E and Fig. S5). Subsequently, a transwell assay and cell scratch assay was conducted to further confirm the impact of mEPC-NV on EC migration. As depicted in Fig. 4B–F and 4C, G and Fig. S5, mEPC-NV markedly enhanced cell migration after 24 h of exposure. Additionally, the tube formation assay revealed enhanced tubular structures with a higher number of tube formations and junction points in the mEPC-NV group under oxidative stress, surpassing both the PBS and EPC-NV groups. (Fig. 4D–H and Fig. S5). These results suggested that mEPC-NVs restore EC proliferation, migration, and tube-forming functions under oxidative stress, which may due to the greater aggregation of functional mEPC-NVs in the vicinity of ECs.

3.5. Preparation and characterization of AFG-mNV hydrogel

Our hydrogel design aims to preserve the natural three-dimensional extracellular matrix structure of ADM and the activity of the internal bioactive factor while enabling antioxidant and antimicrobial properties to sustainably release mNVs for diabetic wound repair. The AFG-mNV hydrogel was synthesized at room temperature (Fig. 5A). Fig. 5B displays the morphologies of the GelMA and AFG-mNV hydrogel. Fig. 5C shows the porous structure of the AFG-mNV hydrogel as visualized by SEM. As shown in Fig. 5D, the mEPC-NV was separated uniformly in the hydrogel. We also tested the degradation rate of the AFG hydrogel, which exceeded 70 % within ten days, reaching the intended target. In addition, a hemolysis test showed that the extent of hemolysis was similar to that of the blood incubated with PBS, with a low percentage of ruptured red blood cells (<5 %) (Fig. 5F and G). Rheological measurements were utilized to evaluate the mechanical properties of the hydrogels. A rheometer was employed to examine the relationship between the energy storage modulus (G') and the loss modulus (G'') of the AFG hydrogel (Fig. 5H). The finding demonstrated that the energy storage modulus of the AFG hydrogel surpassed the loss modulus, suggesting the presence of crosslinking. To confirm that mNVs could be sustainably released from the AFG-mNV hydrogel, daily mNV release was quantified using the microBCA microprotein assay. Approximately 50 % of total mNVs loaded in the AFG-mNV hydrogel were released within five days, and nearly 80 % of mNVs were released within 14 days, indicating that mNVs could be customized release from the hydrogel (Fig. 5I). These findings collectively confirmed the successful synthesis of AFG hydrogel loaded with mEPC-NV.

3.6. Biocompatibility of AFG hydrogel

The application of medical biomaterials relies heavily on superior biocompatibility. Thus, we investigated whether our AFG hydrogel had any cytotoxic effects on HUVEC, HDF, and HaCaT cells by CCK-8 assay and LIVE/DEAD staining. Following incubation with the AFG hydrogel, we identified no cytotoxicity in any of the cell types, with the cell viability remaining above 90 % (Fig. 7S. A and C). To distinguish live cells from dead ones, calcein-AM (green) and propidium iodide (red) stains were used. Additionally, to ensure the absence of cytotoxic effects during hydrogel degradation, the biocompatibility of degradation products from the AFG hydrogel was assessed. As shown in Fig. 7S. B and D, the degradation of the AFG hydrogel was non-toxic and promoted the proliferation of HUVEC, HDF and HaCaT cells. Notably, the degradation solution of the AFG hydrogel and the co-culture of cells with the hydrogel both increased the survival rates of HUVEC, HDF, and HaCaT

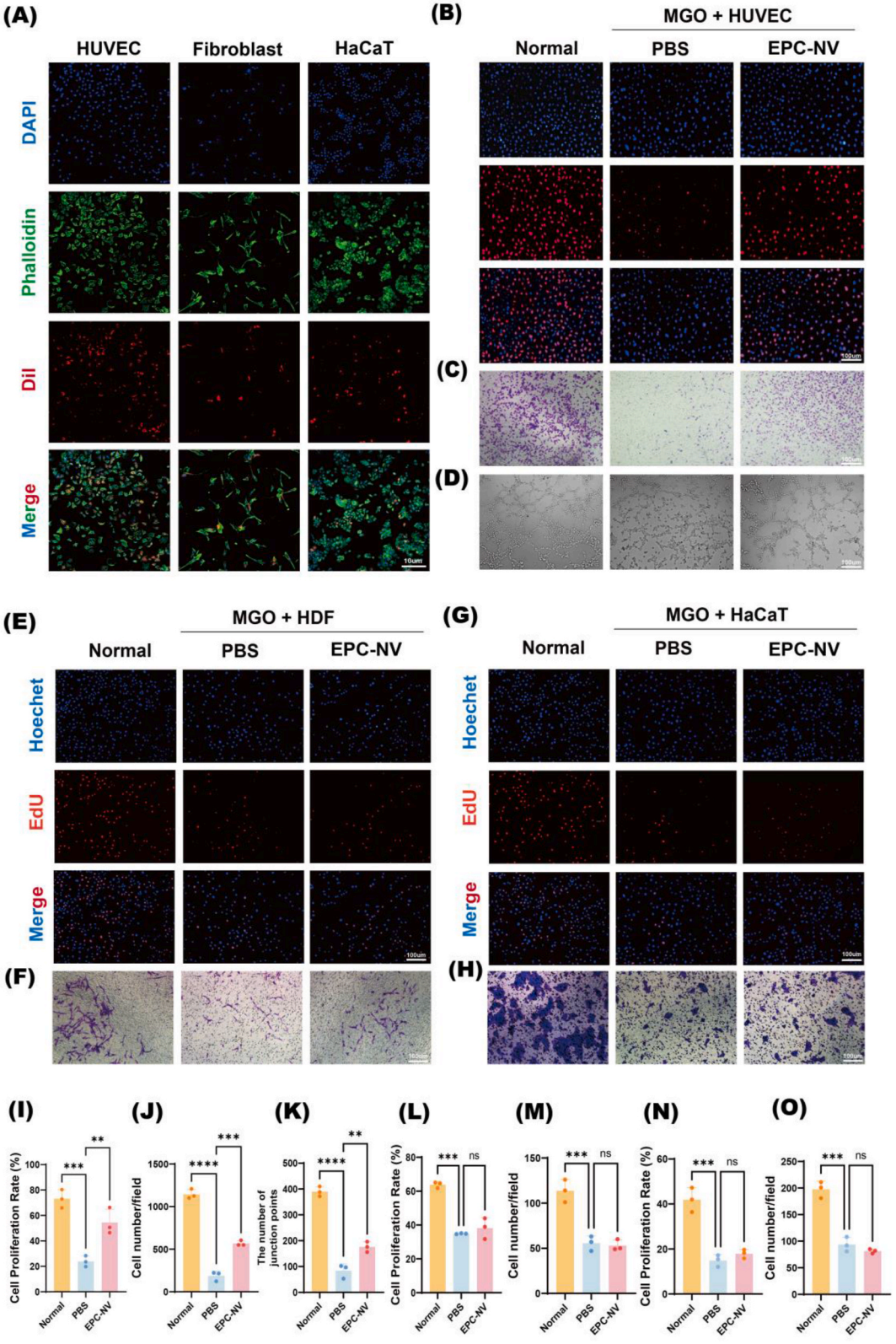

Fig. 2. EPC-NV can promote EC function under oxidative stress.
(A) Internalization of DiI-labeled EPC-NV (red) in HUVEC, HDF, and HaCaT (blue nucleics and green cytoskeletons). Scale bar: 10 μm. **(B)** Representative images of proliferative HUVECs in EdU staining. The proliferative cells were stained with red color, and their cellular nucleis were stained with blue color. Scale bar: 100 μm. **(C)** Representative images of migrating HUVECs in transwell assay. The migrating HUVECs stained purple by crystal violet. Scale bar: 100 μm. **(D)** Representative images of tube formation of HUVECs. Scale bar: 100 μm. **(E, F)** Representative images of proliferative and migrating HDF. Scale bar: 100 μm. **(G, H)** Representative images of proliferative and migrating HaCaT. Scale bar: 100 μm. **(I, J, K)** Statistical analysis of B-D. **(L, M)** Statistical analysis of E, F. **(N, O)** Statistical analysis of G, H. (ns indicates no significant, $^{**}p < 0.01$, $^{***}p < 0.001$, $^{****}p < 0.0001$).

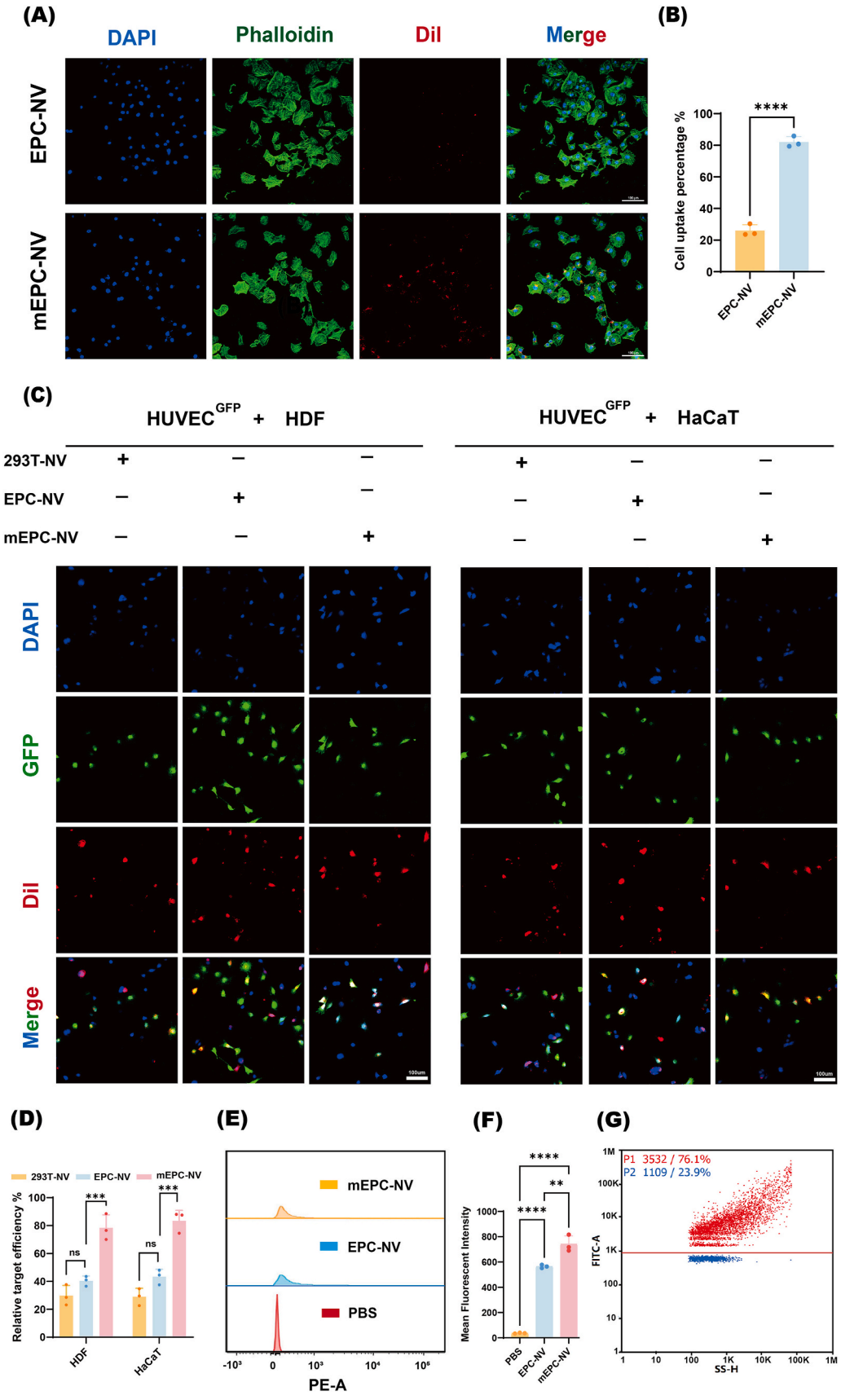

(caption on next page)

Fig. 3. cRGD-modified EPC- NV achieves EC-targeting *in vitro*
(A, B) Representative images and quantification data of internalization of DiI-labeled EPC-NV and DiI-labeled mEPC-NV in HUVECs. Scale bar: 100 μm. **(C)** Validation of mEPC-NV EC-targeting in cutaneous cell model *in vitro*. Scale bar: 100 μm. **(D)** Corresponding statistical analysis of EC target efficiency in different co-culture condition. **(E, F)** Representative images and quantification data of MFI in FCM. **(G)** The positive connectivity between RGD peptides and NVs. (ns indicates no significant, $^{**}p < 0.01$, $^{***}p < 0.001$, $^{****}p < 0.0001$).

cells, as measured by a CCK-8 assay (Fig. 7S. E and F). These findings collectively emphasize the outstanding biocompatibility of our AFG hydrogel.

3.7. Antibacterial and antioxidant ability of AFG hydrogel in vitro

After incubating the bacteria with AFG hydrogel for 4 h, a colony formation assay showed that the AFG hydrogel group markedly reduced the viability of *S. aureus* and *E. coli* (Fig. 6A). Especially, the AFG hydrogel inhibited the survival rate of *S. aureus* and *E. coli* by 70.7 % and 40.5 %, respectively (Fig. 6B). We further investigated bacterial growth after 24 h. In the AFG hydrogel group, the absorbance curve of the bacterial solution was significantly shifted to the right and the peak value decreased (Fig. 6C). Additionally, we conducted a bacterial inhibition ring formation assay, which showed no bacterial growth in the regions of the formed rings, with the diameter of the inhibitory ring measuring approximately 60 % of that of the positive control for *E. Coli* and 50 % for *S. aureus*, respectively (Fig. 6D and E). These results indicated that the AFG hydrogel has sufficient antibacterial properties. Fig. 6F and G shows that the abundance of ROS in HUVEC, HDF, and HaCaT cells was significantly lower within the effect of AFG hydrogel compared to the MGO group ($P < 0.001$), suggesting excellent anti-ROS ability of AFG hydrogel in diabetic wounds. All these results verified the good antibacterial and ROS-reducing abilities of AFG hydrogel in diabetic wound *in vitro*.

3.8. AFG-mNV hydrogel accelerates diabetic wound healing in vivo

To further verify the potential of AFG-mNV hydrogel in the clinic, we established a full-thickness wound model in the dorsum of both normal and diabetic mice and divided them into six groups: untreated normal mice served as a control, and diabetic mice in the remaining 5 groups were treated with PBS, AFG, NV, mNV, and AFG-mNV, respectively (Fig. 7A). As Fig. 7B–E indicate, the wounds of Normal and AFG-mNV mice were completely healed on day 12 post-surgery, while the diabetic wounds treated with PBS exhibited delayed wound healing and were far from complete closure. Notably, at days 4, 8, and 12 post-wounding, the mice treated with AFG-mNV exhibited the lowest rate of unclosed wounds among the various treatment groups, approaching levels observed in the Normal group.

Next, we dissected wound sections of all groups on day 12 post-surgery and carried out downstream histological analysis. H&E and Masson staining analysis showed that AFG, NV, mNV, and AFG-mNV decreased granulation tissue lengths and accelerated collagen deposition of diabetic wounds when compared with those of the PBS group. Both the mNV and AFG-mNV groups demonstrated markedly higher rates of re-epithelialization and collagen deposition, with the AFG-mNV group exhibiting the most significant effect, while the AFG and NV groups demonstrated showed lower re-epithelialization and collagen deposition rates than the mNV and AFG-mNV groups (Fig. 8A–D). Additionally, wounds treated with AFG-mNV exhibited a collagen arrangement closely resembling that of normal wound tissue.

To detect and quantify angiogenesis in wound beds of the different groups, immunofluorescence staining analysis of α-SMA and immunohistochemical staining of CD31 were performed. These analyses highlighted that the AFG-mNV hydrogel group exhibited the highest fluorescence intensity of α-SMA and the highest vascular density, which were even closing the levels observed in the Normal group (Fig. 8E–H).

These findings collectively suggested that ADM-Fe^{3+}@PA and mEPC-NV can synergistically enhance diabetic wound healing *in vivo*. Additionally, AFG-mNV treatment achieved better wound neovascularization than mNV did in diabetic wound healing.

3.9. ROS scavenging, EC-targeting and antibacterial activity of AFG-mNV hydrogel in vivo

To confirm the potential role of inflammation in diabetic wound healing, immunofluorescence staining for IL-1β was conducted. The results indicated evident inflammation in the wound bed within the PBS and NV groups compared with negative control group, whereas inflammation in the AFG and AFG-mNV groups was downregulated (Fig. 9A and B). The ROS levels in the wound were assessed via DHE staining. The intensity of the red fluorescence signal markedly decreased in the AFG-mNV group compared to other groups (Fig. 9C and D). These results indicated that AFG-mNV hydrogel can efficiently diminish the inflammatory response and oxidative stress.

The EC-targeting ability and distribution of mNVs in the diabetic wound were further explored by immunofluorescence examination *in vivo*. As shown in Fig. 9E, compared with the DiI-labeled NV, the DiI-labeled mNV group had a wide distribution (red signal) in diabetic wounds at day 4. Moreover, we noted that mNV showed greater colocalization with blood vessels compared with NV (Fig. 9F). The results showed that mNV could accumulate in ECs efficiently, due to the membrane-modified cRGD-targeted peptides.

The antibacterial activity of AFG-mNV hydrogel was further examined using an *S. aureus* infection wound model *in vivo*. Representative images of infected wounds showed obvious signs of infection and inflammation, such as redness and secretion, by day 0. As expected, the AFG and AFG-mNV groups exhibited the best wound healing throughout the treatment period, with wounds in the AFG-mNV group nearly healed by day 10. (Fig. S8 B-D). The colony formation assay of wound crust and secretion further confirmed the infection progression of infected wounds (Fig. S8 E, F). The results of bacteria quantification *in vivo* verified the successful establishment of infected wounds by day 0. The suppression of bacteria viability in the AFG and AFG-mNV groups further confirmed the antibacterial properties of AFG hydrogel.

4. Discussion

In this study, we successfully prepared biomimetic NVs from EPCs through an extrusion approach. Engineered membrane cRGD-targeting peptides conferred the EC-targeting ability of these EPC-NVs. Furthermore, we successfully designed a multifunctional AFG hydrogel with excellent antioxidant and antibacterial ability to sustainably release mEPC-NVs. The synergistic treatment of AFG hydrogel and mNV showed outstanding efficacy in an *in vivo* model of diabetic wounds.

Impaired EC function induced by high glucose is a key factor in non-healing diabetic wounds. Considering the crucial role of ECs in wound healing, restoring endothelial function in wound tissues offers a potential therapeutic strategy [42,50–52]. EPC-derived EVs promote EC function and increase angiogenesis under hypoxic conditions, attributed to the transfer of pro-angiogenic microRNAs and proteins from the EPC-EVs to recipient ECs [53–55]; however, this technique is associated with low yield and high cost, which limit clinical application. Lately, NVs derived from cell extrusion have gained widespread application as nanocarriers for drug delivery in various disease treatments, owing to their high yields, rapid production, excellent uniformity, and inheritance of parental cell phenotypes [56–60]. Thus, we designed a

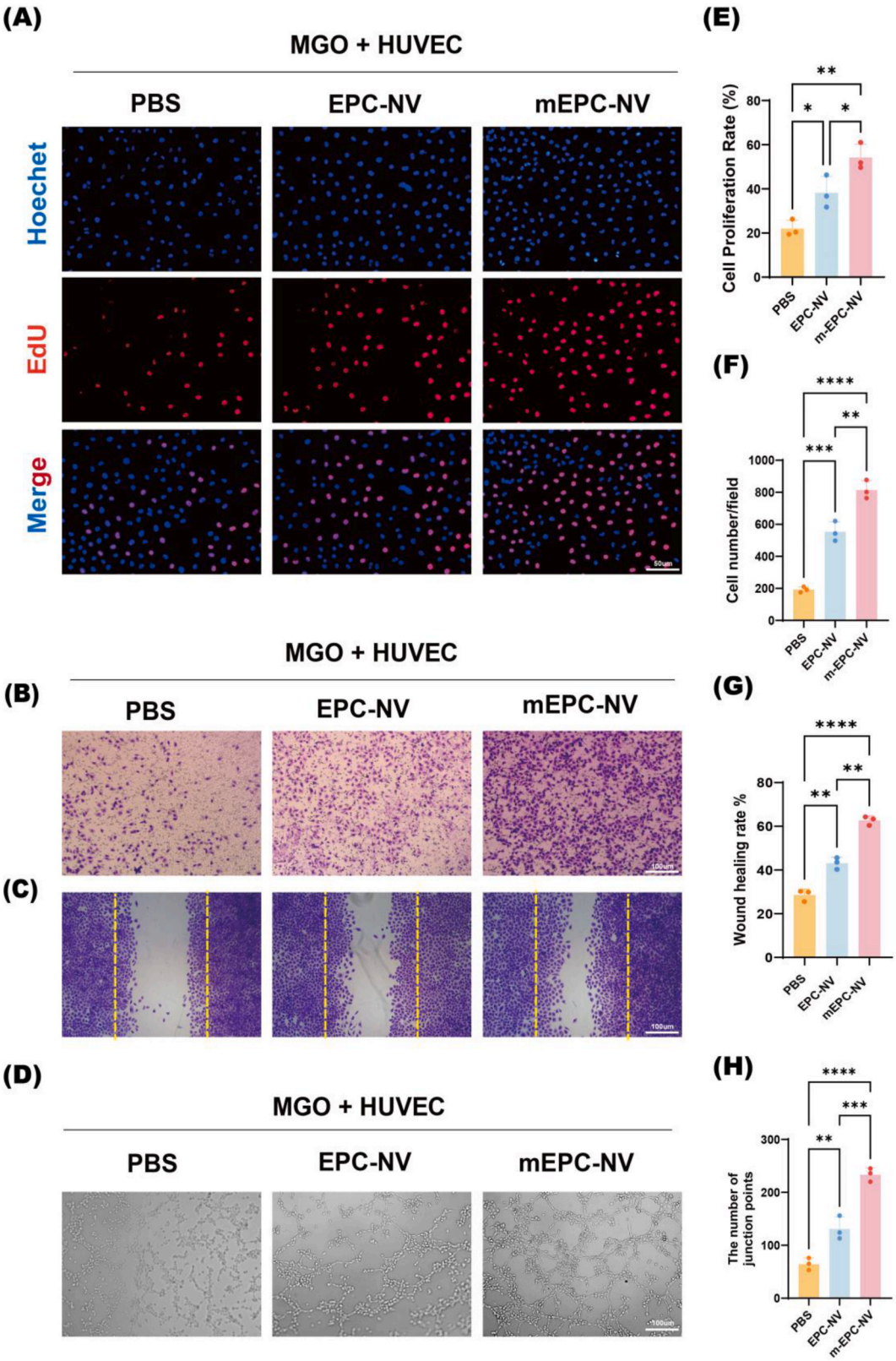

Fig. 4. mEPC-NV restores EC function.
(A, E) Representative images and quantification data of immunofluorescence staining for EdU. Scale bar: 50 μm. **(B, F)** Representative images and quantification of transwell migration for HUVECs. Scale bar: 100 μm. **(C, G)** Scratch assay of HUVECs and corresponding statistical analysis, cells were stained with crystal violet, and the original scratch was labeled by yellow dotted lines. Scale bar: 100 μm. **(D, H)** Representative images and relative quantification of number of junction points of a matrigel tube formation assay. Scale bar: 100 μm. (*$p < 0.05$, **$p < 0.01$, ***$p < 0.001$, ****$p < 0.0001$).

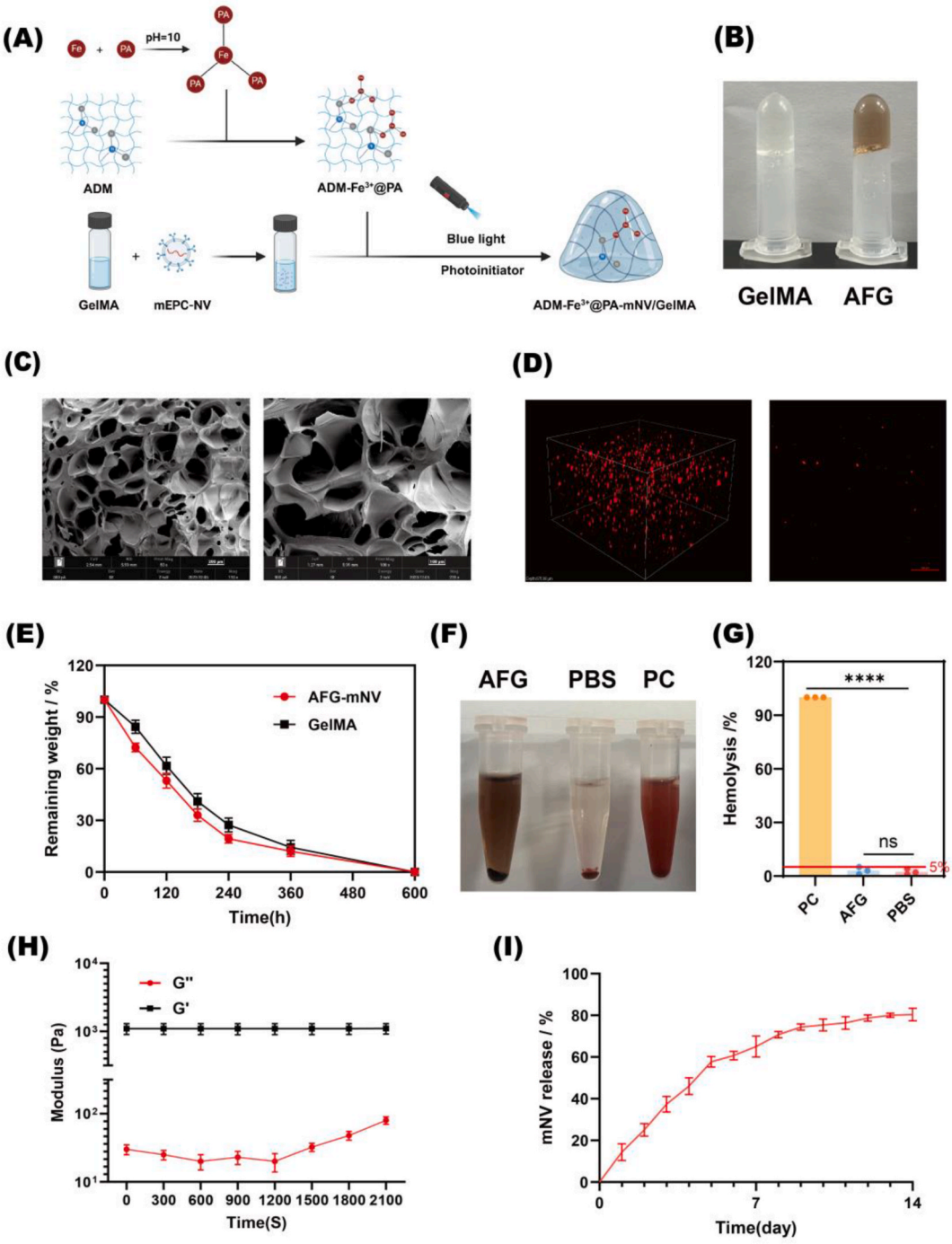

Fig. 5. Preparation and characterization of AFG-mNV hydrogel.
(A) The schematic of hydrogel synthesis. **(B)** Morphologies of GelMA hydrogel and AFG hydrogel. **(C)** SEM image of AFG hydrogel **(D)** Plan and 3D construction image of AFG-mNV hydrogel (mNV was labeled by DiI). scar bar: 100 μm. **(E)** Degradation rate of AFG hydrogel. **(F)** Hemolysis test results and **(G)** quantitative analysis. **(H)** Rheological behavior of the AFG hydrogel. **(I)** The release curve of mNV in the AFG-mNV hydrogel. (ns indicates no significant, ****$p < 0.0001$).

biomimetic NV derived from EPCs to promote diabetic wound healing. Consistent with previously reported results, we found that for the same number of 8 vials of T75 EPC cells, the number of particles obtained by extrusion was about 14 times higher than that obtained by collecting the supernatant (Fig. 6S).

Integrin αvβ3 is widely expressed in a variety of cell types, vascular ECs, vascular smooth muscle cells, platelets, leukocytes, tumor cells, osteocytes, stem cells. The RGD peptide, a ligand for the αvβ3 integrin, has been extensively investigated for targeted therapy of cancer and anti-angiogenic applications but has not been used in EV bioengineering for diabetic wounds [34,37,61–63]. Hence, this study is the first to apply cRGD peptides to diabetic wounds to promote EC-targeting. In our study, both *in vivo* and *in vitro* results consistently demonstrated that cRGD peptide-modified EPC-NV could enhance its uptake by ECs and exhibit a good level of co-localization with EC, thereby avoiding uptake by other cells to optimize EPC-NV function.

ADM is an advanced wound dressing comprising a natural three-dimensional extracellular matrix structure and an array of bioactive factors, which has found extensive clinical applications [64–66]. Furthermore, the degradation products exhibit non-toxicity; therefore, it

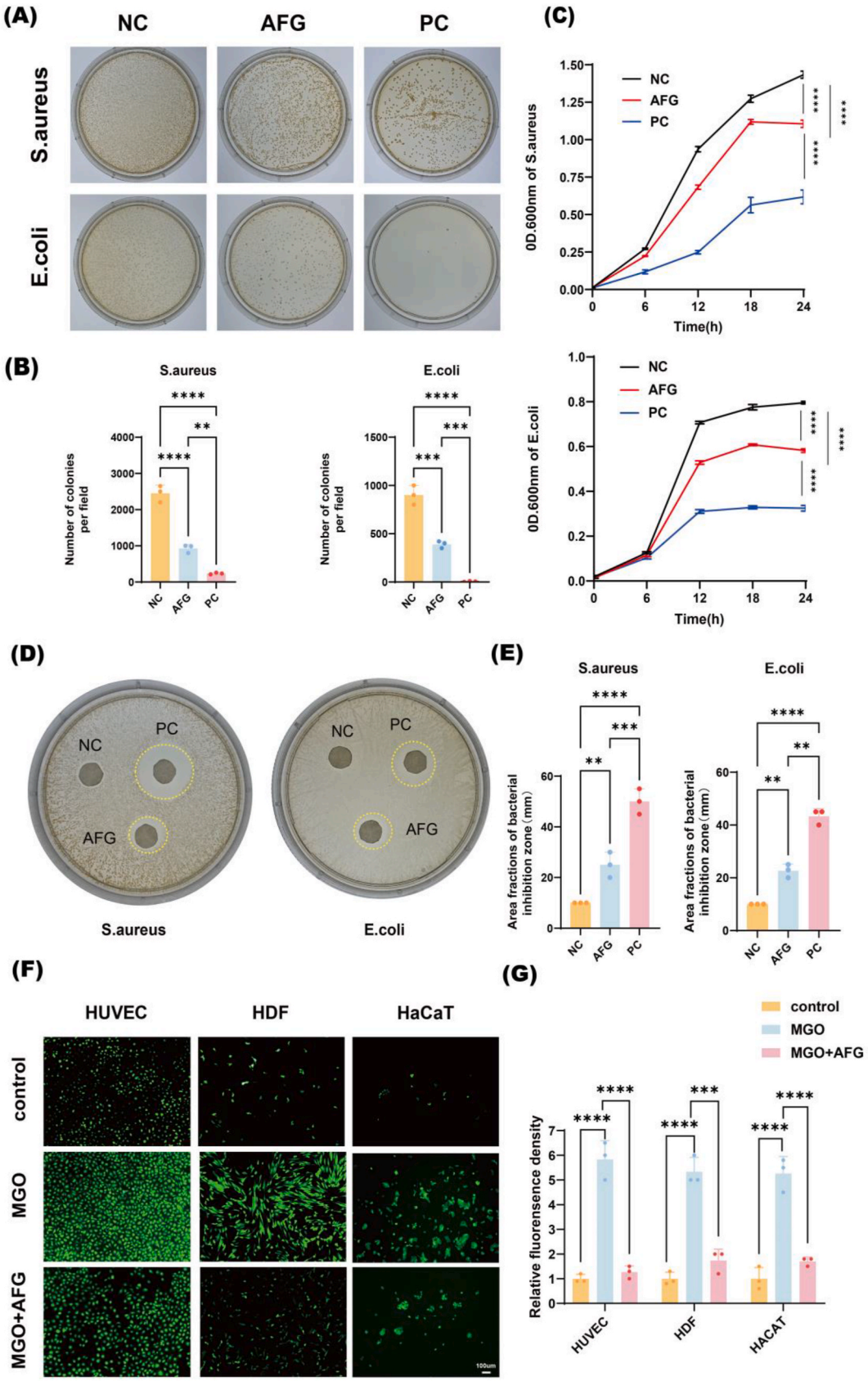

Fig. 6. Antibacterial and antioxidant ability of AFG hydrogel *in vitro*.
(A) Representative images of bacterial clone plate test. **(B)** Statistical analysis of A. **(C)** Bacteria growth curve of *S. aureus* and *E. coli* in 24 h. **(D)** Antibacterial ring of *S. aureus* and *E. coli.* and **(E)** quantitative analysis. **(F)** Level of ROS in HDF, HaCaT and HUVECs, ROS was imaging in green by DCFA-DA probe. scar bar: 100 μm. **(G)** Statistical analysis of F. (**p < 0.01, ***p < 0.001, ****p < 0.0001).

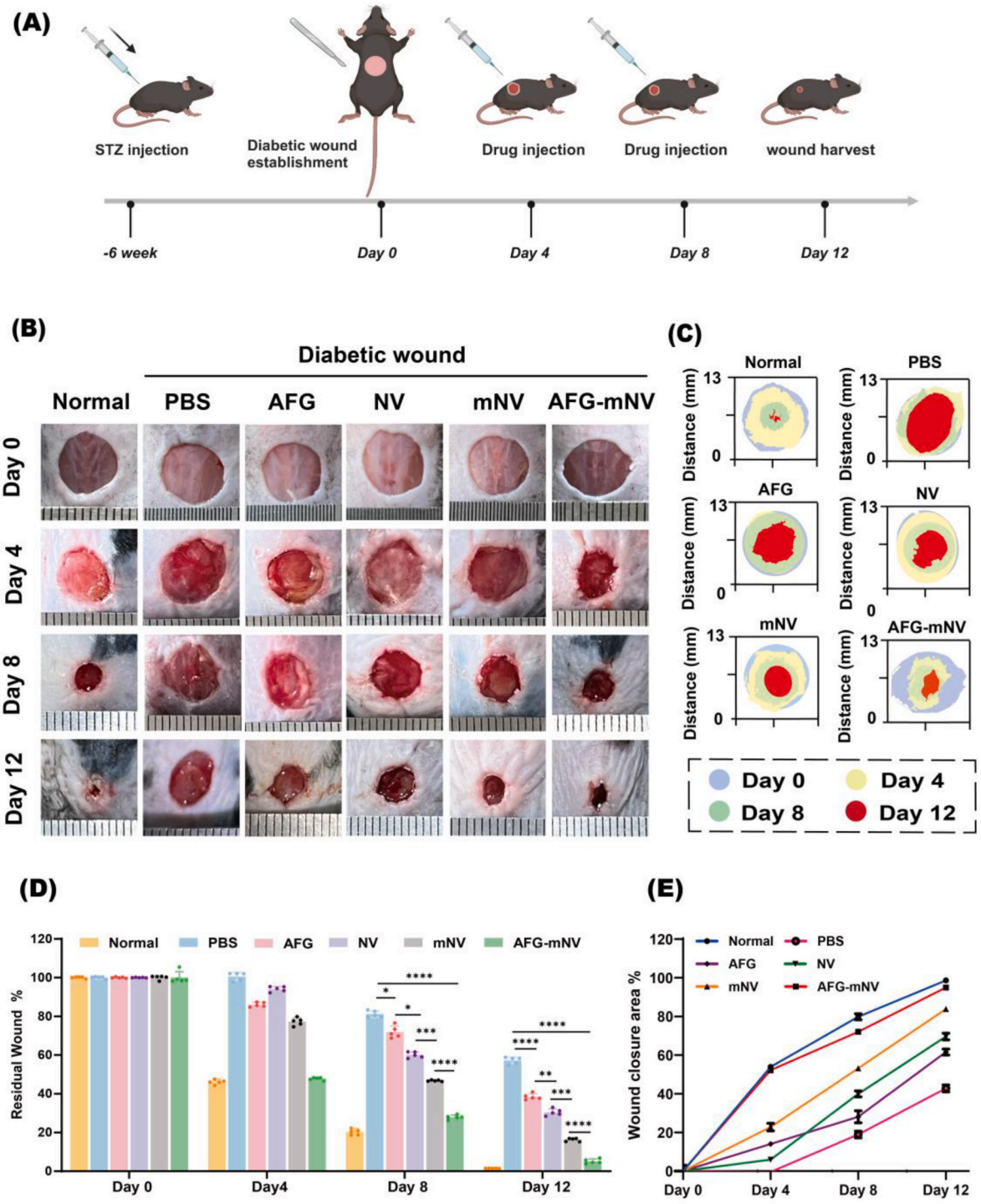

Fig. 7. AFG-mNV hydrogel accelerates diabetic wound healing *in vivo*
(A) Schematic diagram of treated timelines in animal model. **(B)** Gross view of wounds at days 0, 4, 8, 12. **(C)** Images of continuous wound healing trace of each group. **(D)** Statistical analysis of the residual wound area in each group (n = 5). **(E)** Statistical analysis of wound closure area in each group (n = 5). (*p < 0.05, **p < 0.01, ***p < 0.001, ****p < 0.0001).

can self-assemble into a hydrogel to further enhance the therapeutic effect of mEPC-NVs. The dual hydrogel network employs GelMA to enhance the mechanical properties of the hydrogel while preserving the bioactivity of cytokines present in the ADM. PA is a naturally occurring compound renowned for its antibacterial properties and excellent biocompatibility [67,68]. In alkaline conditions at pH = 10, PA could complex with Fe^{3+} forms complexes with a molar ratio of 3:1 via coordination bond, enabling PA to reduce aldehyde group oxidation through physical crosslinking of the catechol moiety with Fe^{3+}. This dynamic crosslinking retains the reductive properties of the complex, endowing it with excellent ROS scavenging capability [69].

Diabetic wounds are highly susceptible to bacterial infections, particularly by *S. aureus* and *E. coli*, posing challenges for effective healing. Moreover, bacterial biofilm formation hinders substance exchange within wounds, further impeding the healing process. Consequently, several studies have advocated for diabetic wound dressings

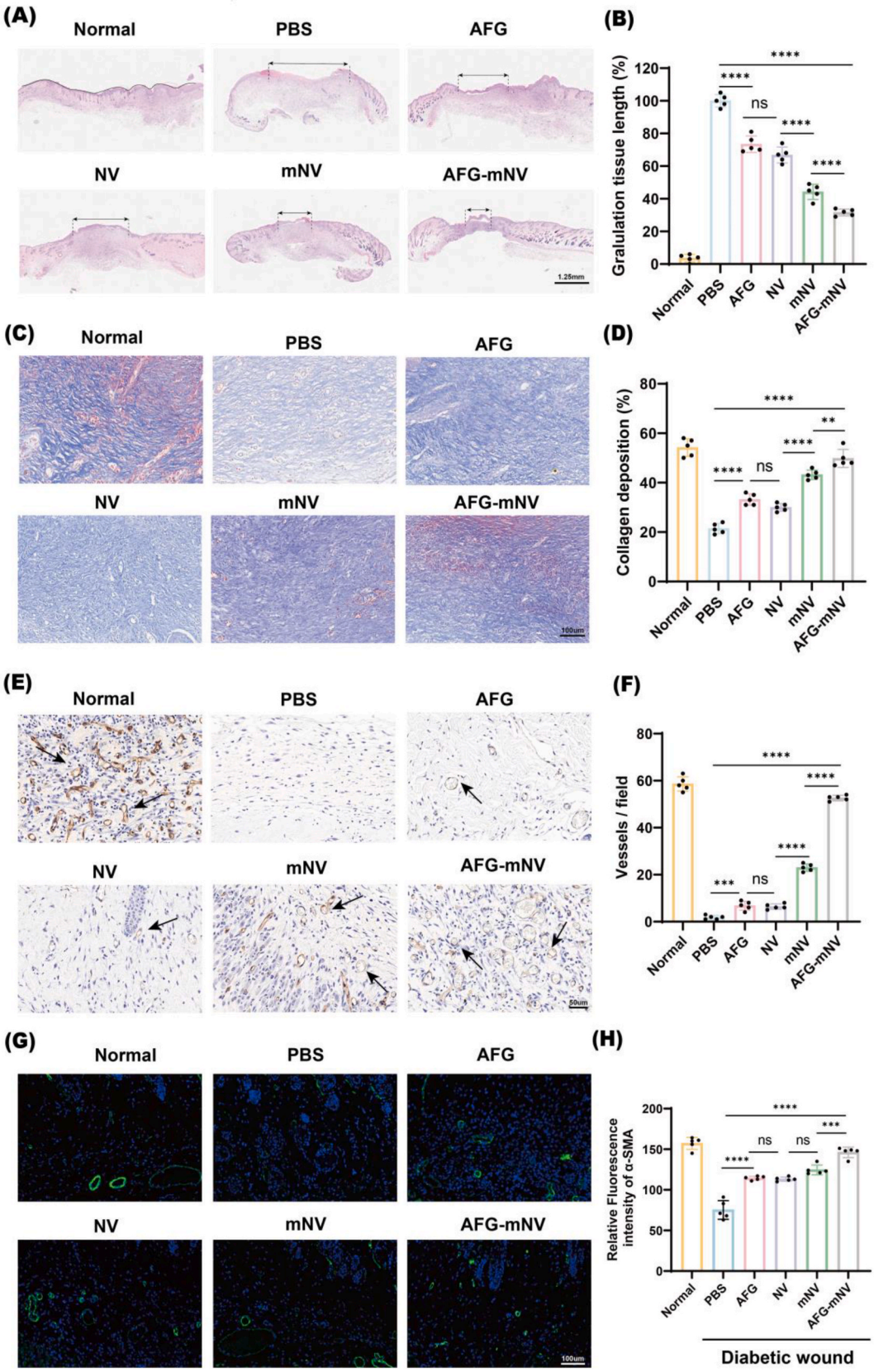

Fig. 8. Histological analysis of diabetic wound healing.
(A) H&E staining of wound sections on day 12 (black double-headed arrows indicates granulation tissue length). scar bar: 1.25 mm. **(B)** Statistical analysis of granulation tissue length (n = 5). **(C)** Masson staining of wound sections on day 12. scar bar: 50 μm. **(D)** Statistical analysis of the stain intensity of blue collagen (n = 5). **(E)** Immunohistochemical staining for CD31 (The arrow indicates neovascularization). scar bar: 50 μm. **(F)** Statistical analysis of vessels field (n = 5). **(G)** Immunofluorescent staining of α-SMA. Smooth muscle cells (α-SMA) and cell nuclei (DAPI) were stained with green and blue, respectively. scar bar: 100 μm. **(H)** Statistical analysis of relative fluorescence intensity (n = 5). (ns indicates no significant, $^{**}p < 0.01$, $^{***}p < 0.001$, $^{****}p < 0.0001$).

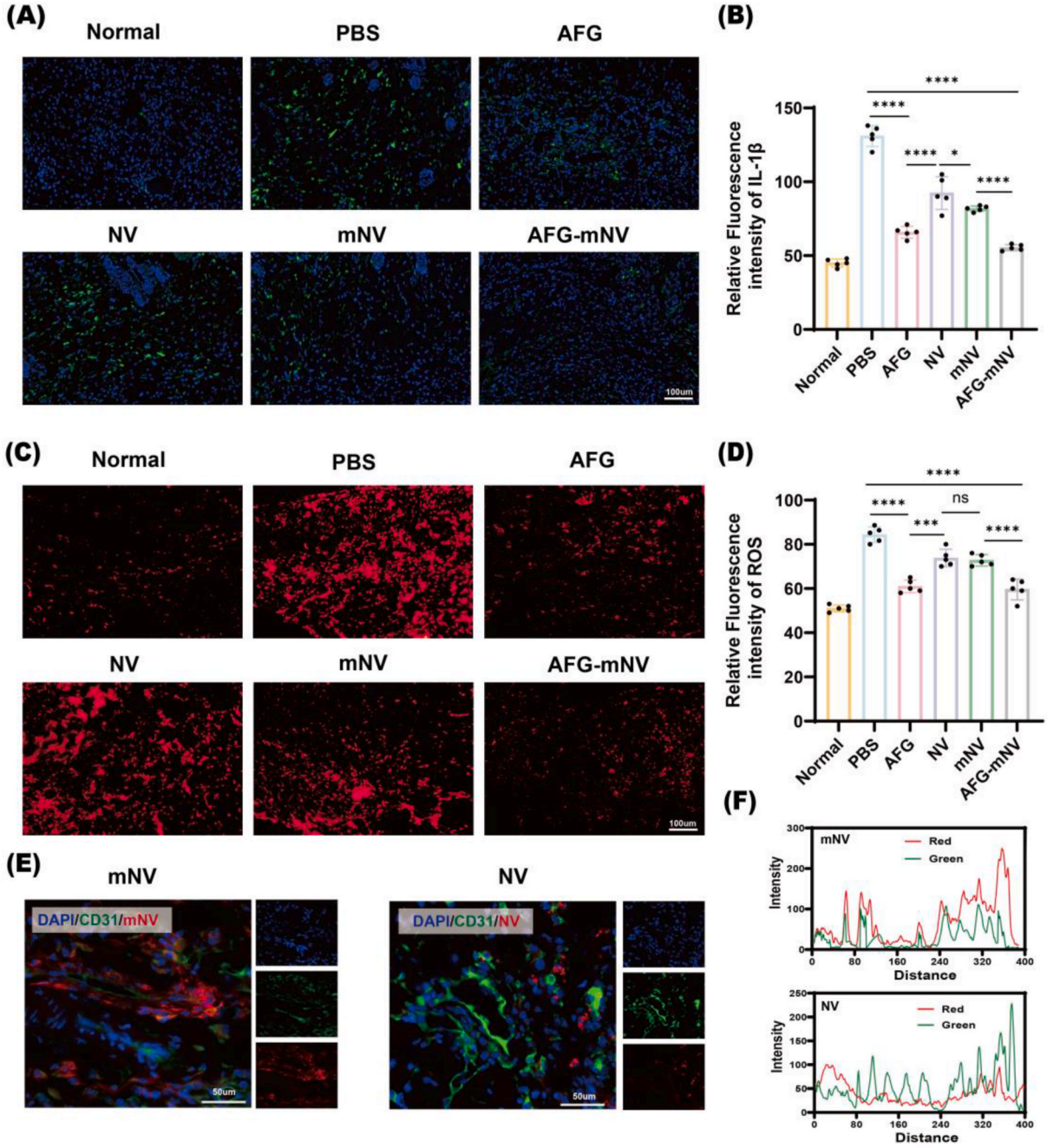

Fig. 9. ROS scavenging and EC-targeting ability of AFG-mNV hydrogel *in vivo*. **(A)** Immunofluorescent staining for IL-1β. IL-1β and cell nuclei (DAPI) were stained with green and blue, respectively. scale bar: 100 μm. **(B)** Statistical analysis of A (n = 5). **(C)** Immunofluorescent staining for DHE. ROS (DHE) and cell nuclei (DAPI) were stained with red and blue, respectively. scale bar: 100 μm. **(D)** Statistical analysis of C (n = 5). **(E)** Immunofluorescence section of diabetic wound on day 4. DiI-labeled mNV, endothelial cells (CD31), and cell nuclei (DAPI) were stained with red, green, and blue, respectively. scale bar: 50 μm. **(F)** Corresponding fluorescence intensity trace in the merged image were plotted. Peak overlapping indicated the co-localization of mNV and CD31. (ns indicates no significant, *$p < 0.05$, ***$p < 0.001$, ****$p < 0.0001$). (For interpretation of the references to color in this figure legend, the reader is referred to the Web version of this article.)

with antimicrobial properties [43,70–72]. In this study, we assessed the *in vitro* antimicrobial efficacy of AFG hydrogel against *S. aureus* and *E. coli*. Compared with the previous results, our AFG hydrogel possessed equally good antibacterial properties of *S. aureus* (70.7 %) and *E. coli* (40.5 %). Given its excellent antimicrobial activity *in vitro*, the hydrogel's therapeutic efficacy was further assessed *in vivo*. On day 10, the bacterial survival rate in the AFG (1.5 %) and AFG-mNV (0.8 %) groups was significantly lower than that in the PBS group (77.5 %). These results suggested that the AFG-mNV hydrogel exhibited excellent antimicrobial properties both *in vitro* and *in vivo*.

Oxidative stress is known to elicit potent inflammation, inhibit angiogenesis, and impair ECs function, consequently delaying wound healing [73]. ROS damages mitochondrial DNA and results in abnormalities in ECs. HDF and HaCaT cell function is also impaired by ROS. Hence, the hydrogel's antioxidant capacity is crucial for enhancing diabetic wound repair. Several studies have shown that PA has antioxidant and antimicrobial properties and is clinically used to treat coronary heart disease, and Fe^{3+} is able to reduce PA oxidation by physically crosslinking catecol groups [74–76]. In this study, we investigated the effects of AFG hydrogel on ROS eliminating both *in vivo* and *in vitro*. We

selected MGO for inducing diabetic cell (HUVEC, HDF, and HaCaT) models. The final concentrations of MGO applied to HUVEC, HDF, and HaCaT cells were 600 μM, 500 μM, and 750 μM, respectively, and the results were obtained from our laboratory [77]. The ROS levels *in vitro* were detected by DCFH assay. In all three cell types, the MGO-only treatment groups exhibited the highest intensity of green fluorescence. After treatment with AFG hydrogel, a significant reduction in ROS levels was observed across the three cell types (HaCaT cells: 3.10 times, HDF: 3.89 times, HUVEC: 4.60 times) compared with the MGO group. The ROS levels *in vivo* were detected by DHE staining. In the AFG-mNV group, red signal was dramatically reduced by about 80 % compared with PBS group. Consistent with previous findings, our results suggested that AFG hydrogel could efficiently reduce ROS, which was due to the antioxidant properties of Fe^{3+}@PA.

5. Conclusion

In summary, the engineered biomimetic mNVs derived from EPCs offer distinct advantages over native EPC-EVs, including higher yields, streamlined manufacturing, and EC-targeting capability that promotes angiogenesis. Notably, the multifunctional AFG hydrogel system incorporating these mNVs synergistically integrates ROS scavenging, antibacterial properties, and angiogenic stimulation, thereby exhibiting a robust capacity to enhance diabetic wound repair. This innovative biomaterial platform, featuring engineered nanovesicles within a multifunctional hydrogel matrix, represents a promising therapeutic modality that harnesses the benefits of biomimicry and multi-pronged activity for efficient management of the complex diabetic wound microenvironment.

CRediT authorship contribution statement

Shuoyuan Liu: Writing – review & editing, Writing – original draft, Software, Methodology, Investigation, Formal analysis, Conceptualization. **Gui Wan:** Methodology, Investigation, Conceptualization. **Tao Jiang:** Methodology, Investigation. **Chengqi Yan:** Methodology, Investigation. **Guoyong Jiang:** Methodology, Investigation. **Maojie Zhang:** Methodology, Investigation. **Kaituo Xiang:** Methodology, Investigation. **Chi Zhang:** Methodology, Investigation. **Xuejiao Xiang:** Methodology, Investigation. **Huayuan Zhao:** Investigation. **Chengcheng Li:** Investigation. **Zhichao Ruan:** Investigation. **Yangyang Chen:** Investigation. **Yanhua Chen:** Supervision, Conceptualization. **Xiaofan Yang:** Supervision, Funding acquisition, Conceptualization. **Zhenbing Chen:** Visualization, Validation, Funding acquisition, Data curation, Conceptualization.

Declaration of competing interest

The authors declare that they have no known competing financial interests or personal relationships that could have appeared to influence the work reported in this paper.

Acknowledgements

This work was supported by the National Natural Science Foundation of China (grant numbers 82370838, 82101473 and 82172221).

Appendix B. Supplementary data

Supplementary data to this article can be found online at https://doi.org/10.1016/j.mtbio.2024.101330.

Data availability

Data will be made available on request.

References

[1] H. Sun, P. Saeedi, S. Karuranga, et al., IDF Diabetes Atlas: global, regional and country-level diabetes prevalence estimates for 2021 and projections for 2045, Diabetes Res. Clin. Pract. 183 (2022) 109119.
[2] M. Chang, T.T. Nguyen, Strategy for treatment of infected diabetic foot ulcers, Acc. Chem. Res. 54 (5) (2021) 1080–1093.
[3] Yang Y, Huang J, Zeng A, et al. The role of the skin microbiome in wound healing [J]. Burns & trauma, 12: tkad059. https://doi.org.10.1093/burnst/tkad059.
[4] L.H. Wang, Y.Y. Wang, L. Liu, et al., From diabetes to diabetic complications: role of autophagy, Curr Med Sci 43 (3) (2023) 434–444, https://doi.org/10.1007/s11596-023-2727-4.
[5] J.L. Burgess, W.A. Wyant, B. Abdo Abujamra, et al., Diabetic wound-healing science, Medicina (Kaunas) 57 (10) (2021), https://doi.org/10.3390/medicina57101072.
[6] Zhou C, Zhang B, Yang Y, et al. Stem cell-derived exosomes: emerging therapeutic opportunities for wou nd healing [J]. Stem Cell Res. Ther., 14(1): 107. https://doi.org.10.1186/s13287-023-03345-0.
[7] Liang Y, He J, Guo B. Functional hydrogels as wound dressing to enhance wound healing [J]. ACS Nano, 15(8): 12687-12722. https://doi.org.10.1021/acsnano.1c04206.
[8] J.G. Powers, C. Higham, K. Broussard, et al., Wound healing and treating wounds: chronic wound care and management, J. Am. Acad. Dermatol. 74 (4) (2016) 607–625, https://doi.org/10.1016/j.jaad.2015.08.070, quiz 25-6.
[9] R.J. Bodnar, Chemokine regulation of angiogenesis during wound healing, Adv. Wound Care 4 (11) (2015) 641–650, https://doi.org/10.1089/wound.2014.0594.
[10] U.A. Okonkwo, L.A. Dipietro, Diabetes and wound angiogenesis, Int. J. Mol. Sci. 18 (7) (2017), https://doi.org/10.3390/ijms18071419.
[11] Q.Z. Chen, Y. Chen, X. Li, et al., TRIB3 interacts with STAT3 to promote cancer angiogenesis, Curr Med Sci 42 (5) (2022) 932–940, https://doi.org/10.1007/s11596-022-2655-8.
[12] Bao S, Tang F, Li X, et al. Epigenetic reversion of post-implantation epiblast to pluripotent embr yonic stem cells [J]. Nature, 461(7268): 1292-1295. https://doi.org.10.1038/nature08534.
[13] J.M. Reinke, H. Sorg, Wound repair and regeneration, Eur. Surg. Res. 49 (1) (2012) 35–43, https://doi.org/10.1159/000339613.
[14] Han Y, Yan J, Li Z-Y, et al. Cyclic stretch promotes vascular homing of endothelial progenitor cell s via Acsl1 regulation of mitochondrial fatty acid oxidation [J]. Proc. Natl. Acad. Sci. U.S.A., 120(6). https://doi.org.10.1073/pnas.2219630120.
[15] Okonkwo U A, Dipietro L A. Diabetes and wound angiogenesis [J]. IJMS, 18(7): 1419. https://doi.org.10.3390/ijms18071419.
[16] Q. Wei, Y. Wang, K. Ma, et al., Extracellular vesicles from human umbilical cord mesenchymal stem cells facilitate diabetic wound healing through MiR-17-5p-mediated enhancement of angiogenesis, Stem Cell Rev Rep 18 (3) (2022) 1025–1040, https://doi.org/10.1007/s12015-021-10176-0.
[17] X. Bian, K. Ma, C. Zhang, et al., Therapeutic angiogenesis using stem cell-derived extracellular vesicles: an emerging approach for treatment of ischemic diseases, Stem Cell Res. Ther. 10 (1) (2019) 158, https://doi.org/10.1186/s13287-019-1276-z.
[18] G. Wan, Y. Chen, J. Chen, et al., Regulation of endothelial progenitor cell functions during hyperglycemia: new therapeutic targets in diabetic wound healing, J. Mol. Med. (Berl.) 100 (4) (2022) 485–498, https://doi.org/10.1007/s00109-021-02172-1.
[19] X. Ke, Z. Liao, X. Luo, et al., Endothelial colony-forming cell-derived exosomal miR-21-5p regulates autophagic flux to promote vascular endothelial repair by inhibiting SIPL1A2 in atherosclerosis, Cell Commun. Signal. 20 (1) (2022) 30, https://doi.org/10.1186/s12964-022-00828-0.
[20] W. Xiong, X.L. Huang, C.Y. Li, et al., Astragaloside IV - mediated endothelial progenitor cell exosomes promote autophagy and inhibit apoptosis in hyperglycemic damaged endothelial cells via miR-21/PTEN axis, Folia Histochem. Cytobiol. 60 (4) (2022) 323–334, https://doi.org/10.5603/FHC.a2022.0030.
[21] Z. Xing, C. Zhao, H. Liu, et al., Endothelial progenitor cell-derived extracellular vesicles: a novel candidate for regenerative medicine and disease treatment, Adv Healthc Mater 9 (12) (2020) e2000255, https://doi.org/10.1002/adhm.202000255.
[22] B. Yang, Y. Lin, Y. Huang, et al., Extracellular vesicles modulate key signalling pathways in refractory wound healing, Burns Trauma 11 (2023) tkad039, https://doi.org/10.1093/burnst/tkad039.
[23] J. Fan, C.S. Lee, S. Kim, et al., Generation of small RNA-modulated exosome mimetics for bone regeneration, ACS Nano 14 (9) (2020) 11973–11984, https://doi.org/10.1021/acsnano.0c05122.
[24] M. Yuan, K. Liu, T. Jiang, et al., GelMA/PEGDA microneedles patch loaded with HUVECs-derived exosomes and Tazarotene promote diabetic wound healing, J. Nanobiotechnol. 20 (1) (2022) 147, https://doi.org/10.1186/s12951-022-01354-4.
[25] L. Cao, T. Tian, Y. Huang, et al., Neural progenitor cell-derived nanovesicles promote hair follicle growth via miR-100, J. Nanobiotechnol. 19 (1) (2021) 20, https://doi.org/10.1186/s12951-020-00757-5.
[26] Y. Jia, L. Yu, T. Ma, et al., Small extracellular vesicles isolation and separation: current techniques, pending questions and clinical applications, Theranostics 12 (15) (2022) 6548–6575, https://doi.org/10.7150/thno.74305.
[27] N. Yom-Tov, R. Guy, D. Offen, Extracellular vesicles over adeno-associated viruses: advantages and limitations as drug delivery platforms in precision medicine, Adv. Drug Deliv. Rev. 190 (2022) 114535, https://doi.org/10.1016/j.addr.2022.114535.

[28] S.C. Jang, O.Y. Kim, C.M. Yoon, et al., Bioinspired exosome-mimetic nanovesicles for targeted delivery of chemotherapeutics to malignant tumors, ACS Nano 7 (9) (2013) 7698–7710, https://doi.org/10.1021/nn402232g.

[29] Y.W. Choo, M. Kang, H.Y. Kim, et al., M1 macrophage-derived nanovesicles potentiate the anticancer efficacy of immune checkpoint inhibitors, ACS Nano 12 (9) (2018) 8977–8993, https://doi.org/10.1021/acsnano.8b02446.

[30] T.H. Stollman, T.J. Ruers, W.J. Oyen, et al., New targeted probes for radioimaging of angiogenesis, Methods 48 (2) (2009) 188–192, https://doi.org/10.1016/j.ymeth.2009.03.006.

[31] A. Sheikh, S. Md, P. Kesharwani, RGD engineered dendrimer nanotherapeutic as an emerging targeted approach in cancer therapy, J. Contr. Release 340 (2021) 221–242, https://doi.org/10.1016/j.jconrel.2021.10.028.

[32] W. Wu, H. Guo, D. Jing, et al., Targeted delivery of PD-L1-derived phosphorylation-mimicking peptides by engineered biomimetic nanovesicles to enhance osteosarcoma treatment, Adv Healthc Mater 11 (23) (2022) e2200955, https://doi.org/10.1002/adhm.202200955.

[33] M. Richter, P. Vader, G. Fuhrmann, Approaches to surface engineering of extracellular vesicles, Adv. Drug Deliv. Rev. 173 (2021) 416–426, https://doi.org/10.1016/j.addr.2021.03.020.

[34] L.M. Knowles, L.A. Gurski, C. Engel, et al., Integrin αvβ3 and fibronectin upregulate Slug in cancer cells to promote clot invasion and metastasis, Cancer Res. 73 (20) (2013) 6175–6184, https://doi.org/10.1158/0008-5472.Can-13-0602.

[35] K.T. Yong, Biophotonics and biotechnology in pancreatic cancer: cyclic RGD-peptide-conjugated type II quantum dots for in vivo imaging, Pancreatology 10 (5) (2010) 553–564, https://doi.org/10.1159/000283577.

[36] S.K. Limoni, M.F. Moghadam, S.M. Moazzeni, et al., Engineered exosomes for targeted transfer of siRNA to HER2 positive breast cancer cells, Appl. Biochem. Biotechnol. 187 (1) (2019) 352–364, https://doi.org/10.1007/s12010-018-2813-4.

[37] X. Wang, Y. Chen, Z. Zhao, et al., Engineered exosomes with ischemic myocardium-targeting peptide for targeted therapy in myocardial infarction, J. Am. Heart Assoc. 7 (15) (2018) e008737, https://doi.org/10.1161/jaha.118.008737.

[38] I.S. Zeelenberg, M. Ostrowski, S. Krumeich, et al., Targeting tumor antigens to secreted membrane vesicles in vivo induces efficient antitumor immune responses, Cancer Res. 68 (4) (2008) 1228–1235, https://doi.org/10.1158/0008-5472.Can-07-3163.

[39] Rosenblum D, Joshi N, Tao W, et al. Progress and challenges towards targeted delivery of cancer therapeuti cs [J]. Nat. Commun., 9(1): 1410. https://doi.org.10.1038/s41467-018-03705-y.

[40] X. Liu, Y. Yang, Y. Li, et al., Integration of stem cell-derived exosomes with in situ hydrogel glue as a promising tissue patch for articular cartilage regeneration, Nanoscale 9 (13) (2017) 4430–4438, https://doi.org/10.1039/c7nr00352h.

[41] Y. Ju, Y. Hu, P. Yang, et al., Extracellular vesicle-loaded hydrogels for tissue repair and regeneration, Mater Today Bio 18 (2023) 100522, https://doi.org/10.1016/j.mtbio.2022.10052. 2.

[42] X. Xiang, J. Chen, T. Jiang, et al., Milk-derived exosomes carrying siRNA-KEAP1 promote diabetic wound healing by improving oxidative stress, Drug Deliv Transl Res 13 (9) (2023) 2286–2296, https://doi.org/10.1007/s13346-023-01306-x.

[43] J. Chen, Y. Liu, G. Cheng, et al., Tailored hydrogel delivering niobium carbide boosts ROS-scavenging and antimicrobial activities for diabetic wound healing, Small 18 (27) (2022) e2201300, https://doi.org/10.1002/smll.202201300.

[44] T. Jiang, S. Liu, Z. Wu, et al., ADSC-exo@MMP-PEG smart hydrogel promotes diabetic wound healing by optimizing cellular functions and relieving oxidative stress, Mater Today Bio 16 (2022) 100365, https://doi.org/10.1016/j.mtbio.2022.100365.

[45] Y. Cui, Z. Li, Y. Guo, et al., Bioinspired nanovesicles convert the skeletal endothelium-associated secretory phenotype to treat osteoporosis, ACS Nano 16 (7) (2022) 11076–11091, https://doi.org/10.1021/acsnano.2c03781.

[46] Yue K, Trujillo-De Santiago G, Alvarez M M, et al. Synthesis, properties, and biomedical applications of gelatin methacry loyl (GelMA) hydrogels [J]. Biomaterials, 73: 254-271. https://doi.org.10.1016/j.biomaterials.2015.08.045.

[47] X. Li, C. Chen, L. Wei, et al., Exosomes derived from endothelial progenitor cells attenuate vascular repair and accelerate reendothelialization by enhancing endothelial function, Cytotherapy 18 (2) (2016) 253–262, https://doi.org/10.1016/j.jcyt.2015.11.009.

[48] Zhang J, Chen C, Hu B, et al. Exosomes derived from human endothelial progenitor cells accelerate Cu taneous wound healing by promoting angiogenesis through erk1/2 signali ng [J]. Int. J. Biol. Sci., 12(12): 1472-1487. https://doi.org.10.7150/ijbs.15514.

[49] J. Wang, S. Chen, J. Bihl, Exosome-Mediated transfer of ACE2 (Angiotensin-Converting Enzyme 2) from endothelial progenitor cells promotes survival and function of endothelial cell, Oxid. Med. Cell. Longev. 2020 (2020) 4213541, https://doi.org/10.1155/2020/4213541.

[50] Qi X, Xiang Y, Cai E, et al. All-in-one: harnessing multifunctional injectable natural hydrogels fo r ordered therapy of bacteria-infected diabetic wounds [J]. Chem. Eng. J., 439: 135691. https://doi.org.10.1016/j.cej.2022.135691.

[51] X. Qi, X. Tong, S. You, et al., Mild hyperthermia-assisted ROS scavenging hydrogels achieve diabetic wound healing, ACS Macro Lett. 11 (7) (2022) 861–867, https://doi.org/10.1021/acsmacrolett.2c00290.

[52] C. Yan, J. Chen, C. Wang, et al., Milk exosomes-mediated miR-31-5p delivery accelerates diabetic wound healing through promoting angiogenesis, Drug Deliv. 29 (1) (2022) 214–228, https://doi.org/10.1080/10717544.2021.2023699.

[53] Xu J, Bai S, Cao Y, et al. <p>miRNA-221-3p in endothelial progenitor cell-derived exosomes accelerates skin wound healing in diabetic mice</p&gt [J]. DMSO, Volume 13: 1259-1270. https://doi.org.10.2147/dmso.s243549.

[54] Salybekov A A, Salybekova A K, Pola R, et al. Sonic hedgehog signaling pathway in endothelial progenitor cell biolog y for vascular medicine [J]. IJMS, 19(10): 3040. https://doi.org.10.3390/ijms19103040.

[55] Yi M, Wu Y, Long J, et al. Exosomes secreted from osteocalcin-overexpressing endothelial progenit or cells promote endothelial cell angiogenesis [J]. Am. J. Physiol. Cell Physiol., 317(5): C932-C941. https://doi.org.10.1152/ajpcell.00534.2018.

[56] Zheng B, Liu Z, Wang H, et al. R11 modified tumor cell membrane nanovesicle-camouflaged nanoparticles with enhanced targeting and mucus-penetrating efficiency for intraves ical chemotherapy for bladder cancer [J]. J. Contr. Release, 351: 834-846. https://doi.org.10.1016/j.jconrel.2022.09.055.

[57] VáZQUEZ-RíOS A J, Molina-Crespo Á, Bouzo B L, et al. Exosome-mimetic nanoplatforms for targeted cancer drug delivery [J]. J. Nanobiotechnol., 17(1). https://doi.org.10.1186/s12951-019-0517-8.

[58] Zhang W, Wang L, Guo H, et al. Dapagliflozin-loaded exosome mimetics facilitate diabetic wound healin g by HIF-1α-Mediated enhancement of angiogenesis [J]. Adv. Healthcare Mater., 12(7). https://doi.org.10.1002/adhm.202202751.

[59] Neupane Y R, Handral H K, Alkaff S A, et al. Cell-derived nanovesicles from mesenchymal stem cells as extracellular vesicle-mimetics in wound healing [J]. Acta Pharm. Sin. B, 13(5): 1887-1902. https://doi.org.10.1016/j.apsb.2022.10.022.

[60] Wen Y, Fu Q, Soliwoda A, et al. Cell-derived nanovesicles prepared by membrane extrusion are good subs titutes for natural extracellular vesicles [J]. Extracell Vesicle, 1: 100004. https://doi.org.10.1016/j.vesic.2022.100004.

[61] Y. Tian, S. Li, J. Song, et al., A doxorubicin delivery platform using engineered natural membrane vesicle exosomes for targeted tumor therapy, Biomaterials 35 (7) (2014) 2383–2390, https://doi.org/10.1016/j.biomaterials.2013.11.083.

[62] S. Ohno, M. Takanashi, K. Sudo, et al., Systemically injected exosomes targeted to EGFR deliver antitumor microRNA to breast cancer cells, Mol. Ther. 21 (1) (2013) 185–191, https://doi.org/10.1038/mt.2012.180.

[63] D. Rosenblum, N. Joshi, W. Tao, et al., Progress and challenges towards targeted delivery of cancer therapeutics, Nat. Commun. 9 (1) (2018) 1410, https://doi.org/10.1038/s41467-018-03705-y.

[64] X. Guo, D. Mu, F. Gao, Efficacy and safety of acellular dermal matrix in diabetic foot ulcer treatment: a systematic review and meta-analysis, Int. J. Surg. 40 (2017) 1–7, https://doi.org/10.1016/j.ijsu.2017.02.008.

[65] M. Climov, L.R. Bayer, A.V. Moscoso, et al., The role of dermal matrices in treating inflammatory and diabetic wounds, Plast. Reconstr. Surg. 138 (3 Suppl) (2016), https://doi.org/10.1097/prs.0000000000002652.

[66] F. Campitiello, M. Mancone, M. Cammarota, et al., Acellular dermal matrix used in diabetic foot ulcers: clinical outcomes supported by biochemical and histological analyses, Int. J. Mol. Sci. 22 (13) (2021), https://doi.org/10.3390/ijms22137085.

[67] Li S, Yu Y, Chen J, et al. Evaluation of the antibacterial effects and mechanism of action of pro tocatechualdehyde against ralstonia solanacearum [J]. Molecules, 21 (6): 754. https://doi.org.10.3390/molecules21060754.

[68] Li M, Wang H, Hu J, et al. Smart hydrogels with antibacterial properties built from all natural B uilding blocks [J]. Chem. Mater., 31(18): 7678-7685. https://doi.org.10.1021/acs.chemmater.9b02547.

[69] Y. Liang, Z. Li, Y. Huang, et al., Dual-dynamic-bond cross-linked antibacterial adhesive hydrogel sealants with on-demand removability for post-wound-closure and infected wound healing, ACS Nano 15 (4) (2021) 7078–7093, https://doi.org/10.1021/acsnano.1c00204.

[70] G. Jiang, J. Guo, C. Yan, et al., Biomimetic hybrid nanovesicles improve infected diabetic wound via enhanced targeted delivery, J. Contr. Release 365 (2024) 193–207, https://doi.org/10.1016/j.jconrel.2023.11.019.

[71] Wang C, Wang M, Xu T, et al. Erratum: engineering bioactive self-healing antibacterial exosomes hyd rogel for promoting chronic diabetic wound healing and complete skin R egeneration: erratum [J]. Theranostics, 11(20): 10174-10175. https://doi.org.10.7150/thno.68432.

[72] Guo Y, Ding S, Shang C, et al. Multifunctional PtCuTe nanosheets with strong ROS scavenging and ROS-I ndependent antibacterial properties promote diabetic wound healing [J]. Adv. Mater., 36(8). https://doi.org.10.1002/adma.202306292.

[73] Wang Z, Zhao F, Xu C, et al. Metabolic reprogramming in skin wound healing [J]. Burns & trauma, 12: tkad047. https://doi.org.10.1093/burnst/tkad047.

[74] Fan L, He Z, Peng X, et al. Injectable, intrinsically antibacterial conductive hydrogels with self -healing and pH stimulus responsiveness for epidermal sensors and woun d healing [J]. ACS Appl. Mater. Interfaces, 13(45): 53541-53552. https://doi.org.10.1021/acsami.1c14216.

[75] Park H-J, Jin Y, Shin J, et al. Catechol-Functionalized hyaluronic acid hydrogels enhance angiogenesis and osteogenesis of human adipose-derived stem cells in critical tiss ue defects [J]. Biomacromolecules, 17(6): 1939-1948. https://doi.org.10.1021/acs.biomac.5b01670.

[76] Zhang W, Wang R, Sun Z, et al. Catechol-functionalized hydrogels: biomimetic design, adhesion mechani sm, and biomedical applications [J]. Chem. Soc. Rev., 49 (2): 433-464. https://doi.org.10.1039/c9cs00285e.

[77] Zhang C, Jiang T, Jiang G, et al. White adipose tissue-derived small extracellular vesicles: a new poten tial therapeutic reagent for accelerating diabetic wound healing [J]. FASEB J, 37(12): e23314. https://doi.org.10.1096/fj.202301549R.